A Platinum Open Access Journal
for Organic Chemistry

Paper

Free to Authors and Readers

DOAJ Seal

Arkivoc **2024** (3) 202412190

Complex-assisted PtZn alloy formation for propane dehydrogenation

Chaokai Xu,[a] Bingqing Yao,[a] and Qian He[a,*]

[a] *Department of Material Science and Engineering, College of Design and Engineering, National University of Singapore, 9 Engineering Drive 1, EA #03-09, 117575, Singapore*
Email: mseheq@nus.edu.sg

This work is dedicated to Professor Graham Hutchings, in recognition of his illustrious career marked by remarkable achievements in heterogeneous catalysis, particularly on developing novel nanoalloy catalysts. The authors also wish to express sincere gratitude for the mentorship and support received from Professor Hutchings

Received 02-26-2024 **Accepted Manuscript** 06-20-2024 **Published on line** 07-01-2024

Abstract

An oxalate-bridged Pt-Zn complex was utilized as metal precursor to improve an impregnation method, producing size-controlled alloy nanoparticles on SiO_2 support for a propane dehydrogenation reaction. FTIR verified the structure of Pt-Zn complex, and enhanced alloy formation was evidenced by TPR and CO-DRIFTS. Compared with the sample prepared by conventional co-impregnation method, a 40% higher space time yield of propylene was achieved over the complex-derived PtZn/SiO_2 catalyst. These findings suggest that using molecular complexes as precursors could be a powerful tool in future pursuit of controlled alloy nanoparticle synthesis, of application in catalytic processes such as propane dehydrogenation.

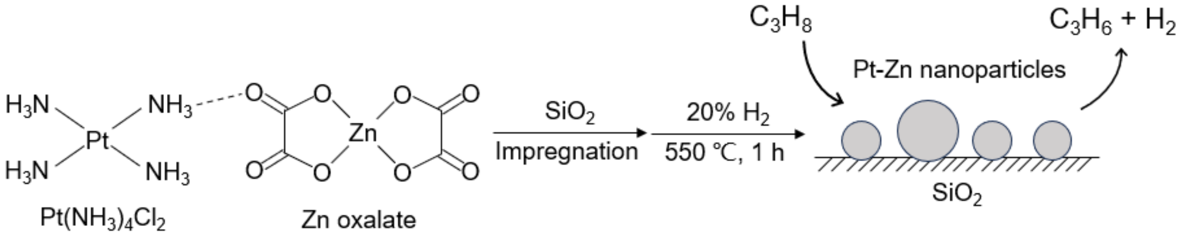

Keywords: Nanoalloy, molecular complex, size control, propane dehydrogenation

Introduction

Alloyed nanoparticles have widespread applications in various catalytic processes, owing to the thorough exposure of active metal species to reactants and promotional effects from additional elements, *e.g.*, site isolation,[1] electronic structure modification[2] and agglomeration inhibition.[3] A conventional approach to synthesizing alloyed nanoparticles involves impregnating metal precursors onto supports, followed by heat treatment in reductive atmosphere to enable alloy formation.[4, 5] While the impregnation method is simple and straightforward, it lacks control over the loading process of multiple metal species. Furthermore, the resultant random distribution of elements sometimes results in insufficient alloy formation during reduction and particle sintering at elevated temperatures.[6]

Non-oxidative dehydrogenation of propane (C_3H_8) to propylene (C_3H_6) is an important industrial process that relies on alloyed nanoparticles, particularly Pt-based catalysts.[7] Pt is capable of activating C-H bonds, thus facilitating the conversion of propane. The close proximity of Pt sites, however, may give rise to side reactions, and failing to desorb products can lead to coke formation. The strategy of alloying is helpful in isolating Pt sites in order to mitigate side reactions and induce charge transfer to Pt for preferential propylene desorption.[8] Fortunately, it is not difficult to prepare Pt-based alloys from metal precursors for this purpose. The operating temperature of the propane dehydrogenation process usually exceeds 500 ℃, due to its highly endothermic character (C_3H_8=C_3H_6+H_2 ΔH=124 kJ/mol).[7] Prior to reaction, the metal species typically undergo H_2 treatment at a temperature equal to or higher than the reaction temperature to allow alloy formation and to stabilize their structures.[5] In addition, the reduction of promoters benefits from the hydrogen spillover effect of Pt sites,[9] so that the alloying between Pt and promoter can be established, while some promoters loaded far away may not get involved in the process.

The potential promoters for Pt have been intensively investigated, *e.g.*, Sn,[5] Zn,[4, 10, 11] Ga[12] and La.[13] Notably, Pt-Zn alloy nanoparticles are anticipated to exhibit outstanding propylene selectivity,[14] which was affirmed by the impressive catalytic performance of Pt-Zn catalysts reported in recent years.[4, 10, 11] Considering the feasibility of catalyst synthesis, it would make Pt-Zn catalysts more applicable if the alloying between Pt and Zn could be enhanced based on a simple impregnation process. Bimetallic complexes, recognized as promising precursors for generating alloyed nanoparticles, offer well-defined structures that elevate the likelihood of interaction between the two elements.[5, 15] Constructing a linkage between Pt and Zn, rather than merely mixing the precursors, is expected to augment alloy formation in heat treatment.

In this work, we used oxalate-bridged Pt-Zn complex as the precursor to refine the control over metal species during the impregnation process. Spectroscopic characterizations confirmed complex formation and improved alloying of Pt-Zn during H_2 reduction, compared with the control sample with simply mixed precursors. While the size distribution of small particles appeared similar in both PtZn/SiO_2 catalysts, the enhanced charge transfer from Zn to Pt contributed to the catalytic performance in the propane dehydrogenation reaction. Consequently, a 30% higher conversion of propane was achieved over the complex-derived PtZn/SiO_2 catalyst. The amount of co-feeding H_2 proved crucial for the reaction, as the facilitated propylene desorption needed to be balanced with respect to the lowered thermodynamic limit.

Results and Discussion

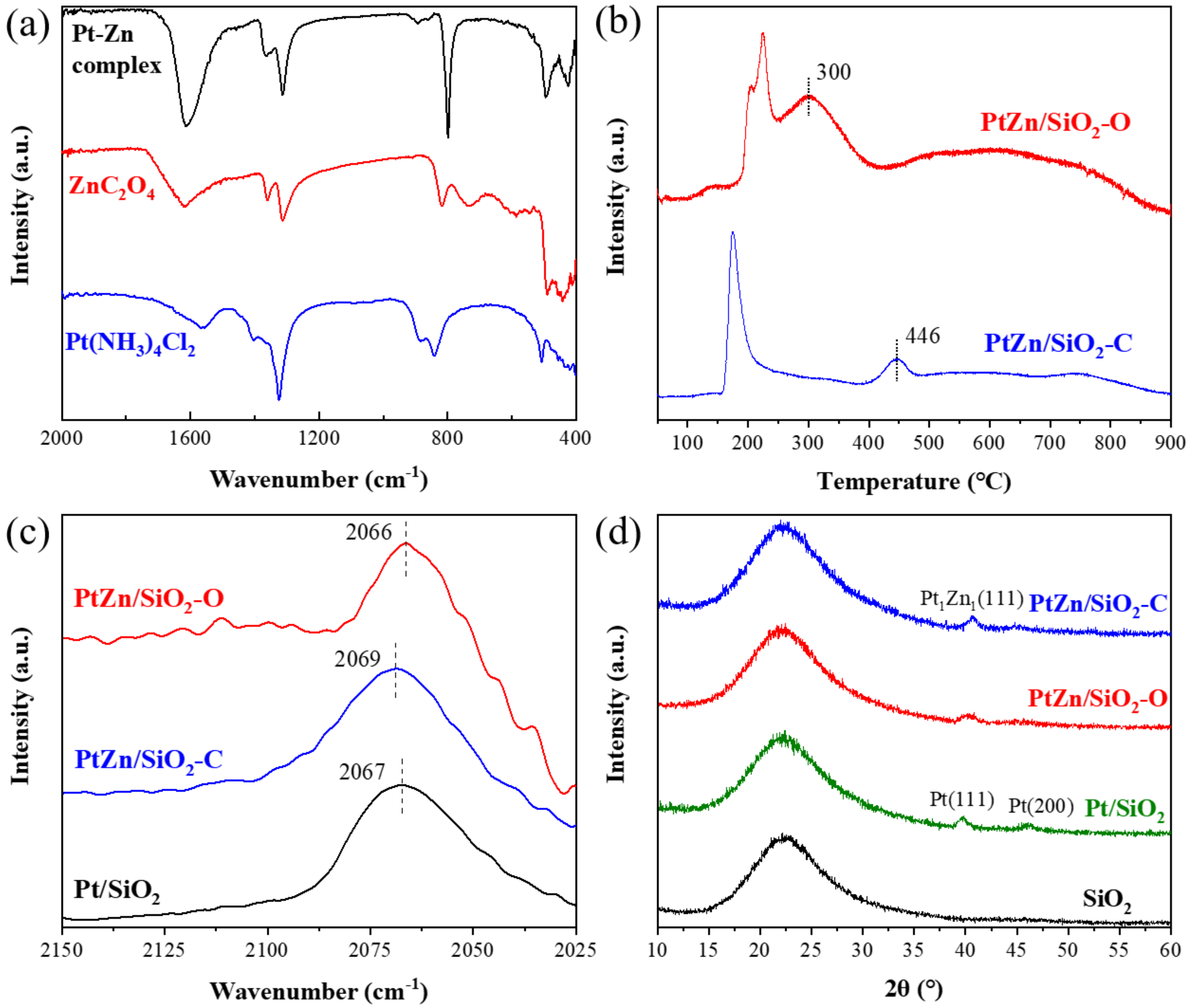

Figure 1. (a) FTIR spectra of $Pt(NH_3)_4Cl_2$, ZnC_2O_4 and oxalate-bridged Pt-Zn complex. (b) TPR patterns of PtZn/SiO_2-O and PtZn/SiO_2-C catalysts. (c) CO-DRIFTS of reduced Pt/SiO_2, PtZn/SiO_2-C and PtZn/SiO_2-O catalysts. (d) XRD patterns of SiO_2 support and reduced catalysts.

The oxalate-bridged Pt-Zn complex was synthesized following the method reported by Zadesenets *et al*.[16] The metal precursors and the bridging agent experienced repeated precipitation-redissolution processes in aqueous solution, and the precipitates in each step, *i.e*., ZnC_2O_4 and Pt-Zn complex, were collected for FTIR analysis together with Pt precursor $Pt(NH_3)_4Cl_2$ (Figure 1a). In the spectra of $Pt(NH_3)_4Cl_2$, peaks at 1566 and 1325 cm^{-1} could be assigned to δ(H-N-H). Another two peaks at 841 and 507 cm^{-1} originated from ρ(H-N-H) and ν(Pt-N), respectively.[17, 18] The structure of ZnC_2O_4 was verified by the peaks at 1622, 1361, 1313 and 818 cm^{-1}, corresponding to ν_{as}(C-O), ν_s(C-O), δ(O-C-O) and ν_s(C-C), respectively.[19] The pattern of Pt-Zn complex was comprised of the features belonging to ZnC_2O_4 and $Pt(NH_3)_4Cl_2$, *e.g.*, the peaks at 1615, 1363, 1313, 894, 861 and 798 cm^{-1}, confirming the co-existence of Pt, Zn and oxalate in the precipitate.[16] Notably, no precipitation could be observed without the bridging agent oxalate. Therefore, the precipitation behavior and FTIR results suggested the formation of oxalate-bridged Pt-Zn complex.

After redissolving the complex and loading it onto a SiO_2 support through an impregnation method, the Pt-Zn species underwent heat treatment in 20% H_2/Ar atmosphere to form the respective alloy. The reduction process was characterized by TPR (Figure 1b). PtZn/SiO_2-C, the control sample prepared by a co-impregnation method, displayed separate reduction processes of Pt (occurring before 200 ℃) and Zn (peak centered at 446 ℃).[20, 21] In comparison, the complex-derived Pt-Zn/SiO_2-O sample exhibited overlapping peaks, ranging from 200 ℃ to 400 ℃, corresponding to oxalate decomposition and co-reduction of Pt and Zn. The reduction temperature of Zn in PtZn/SiO_2-O (peak centered at 300 ℃) was significantly lower than that in PtZn/SiO_2-C, which could be ascribed to the enhanced intimacy between Pt and Zn within the oxalate-bridged structure. Moreover, the relative intensity of the Zn reduction peak compared to the Pt reduction peak implied that more Zn got reduced in PtZn/SiO_2-O compared to PtZn/SiO_2-C. The phenomenon was further verified by the CO-DRIFT spectra of the catalysts after reduction (Figure 1c). Since a larger portion of Zn was reduced in PtZn/SiO_2-O than in PtZn/SiO_2-C, the increased charge transfer from Zn to Pt in the alloy structures led to a red shift of the linearly adsorbed CO peak,[2, 22] from 2069 cm^{-1} to 2066 cm^{-1}.

The as-synthesized Pt-Zn alloy structures were subsequently studied with XRD (Figure 1d). Aside from the SiO_2 peak, the features of ordered Pt could be identified in reduced Pt/SiO_2.[4] As for the reduced PtZn/SiO_2 samples, the Pt peak shifted to higher degrees because of alloy formation (Figure S1). Interestingly, though the predominant Pt_1Zn_1 peak of PtZn/SiO_2-C seemed to represent complete alloying between Pt and Zn, it was contradictory to previous TPR and CO-DRIFTS results. The fraction of reduced Zn and the amount of electrons donated to Pt were smaller in PtZn/SiO_2-C than in PtZn/SiO_2-O. Therefore, the actual Zn/Pt ratio in the nanoparticles should be significantly lower than for PtZn/SiO_2-C. This discrepancy could arise from structural variations in the nanoparticles. With the decrease in size, nanoparticles were likely to become amorphous, rendering them undetectable by XRD.[23] While the ordered structure of larger particles yielded XRD signals, they may contribute minimally to catalytic activity due to limited Pt exposure. To discern the real status of the catalysts, electron microscopy studies were subsequently carried out.

HAADF-STEM images and corresponding particle size distribution unveiled the morphology of metal nanoparticles after reduction (Figure 2 and Figures S2-4). Across all the catalysts, the prevailing species were amorphous particles with diameters around 1 nm, accompanied by a few 2-5 nm sized particles. EDS analysis of individual particles confirmed the alloy formation between Pt and Zn (Figure S5). Ordered structures started to emerge when particle size exceeded 2 nm (Figure S6). Occasionally, large particles (> 10 nm) could be found, which were not included in the above statistical analysis. EDS and measured lattice spacing proved that large particles could contribute to XRD signals (Figure S7), but these features did not accurately represent the overall extent of the alloying process.

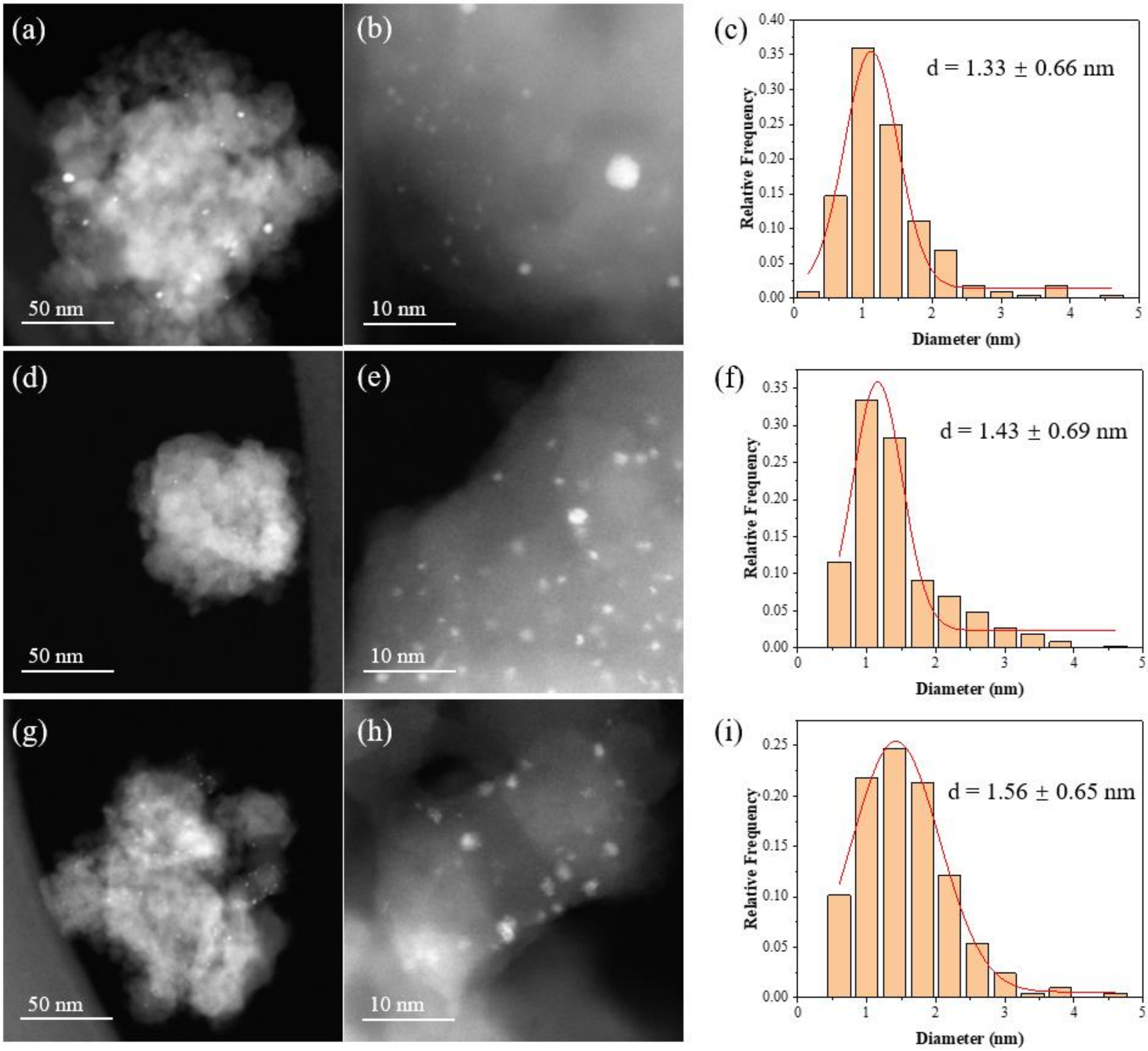

Figure 2. Representative HAADF-STEM images and corresponding particle size distribution of reduced catalysts. (a-c) PtZn/SiO_2-O, (d-f) PtZn/SiO_2-C and (g-i) Pt/SiO_2.

According to the size distribution of small particles in Figure 2 and the frequency of encountering undesired big particles, as shown by SEM-BSE images in Figures S8-10, there was no significant difference in particle sizes among the three samples, despite the introduction of Zn. Integrating the morphological information and spectra in Figure 1, the primary advantages of using oxalate-bridged complex as precursor lay in enhancing alloying and promoting charge transfer from Zn to Pt.

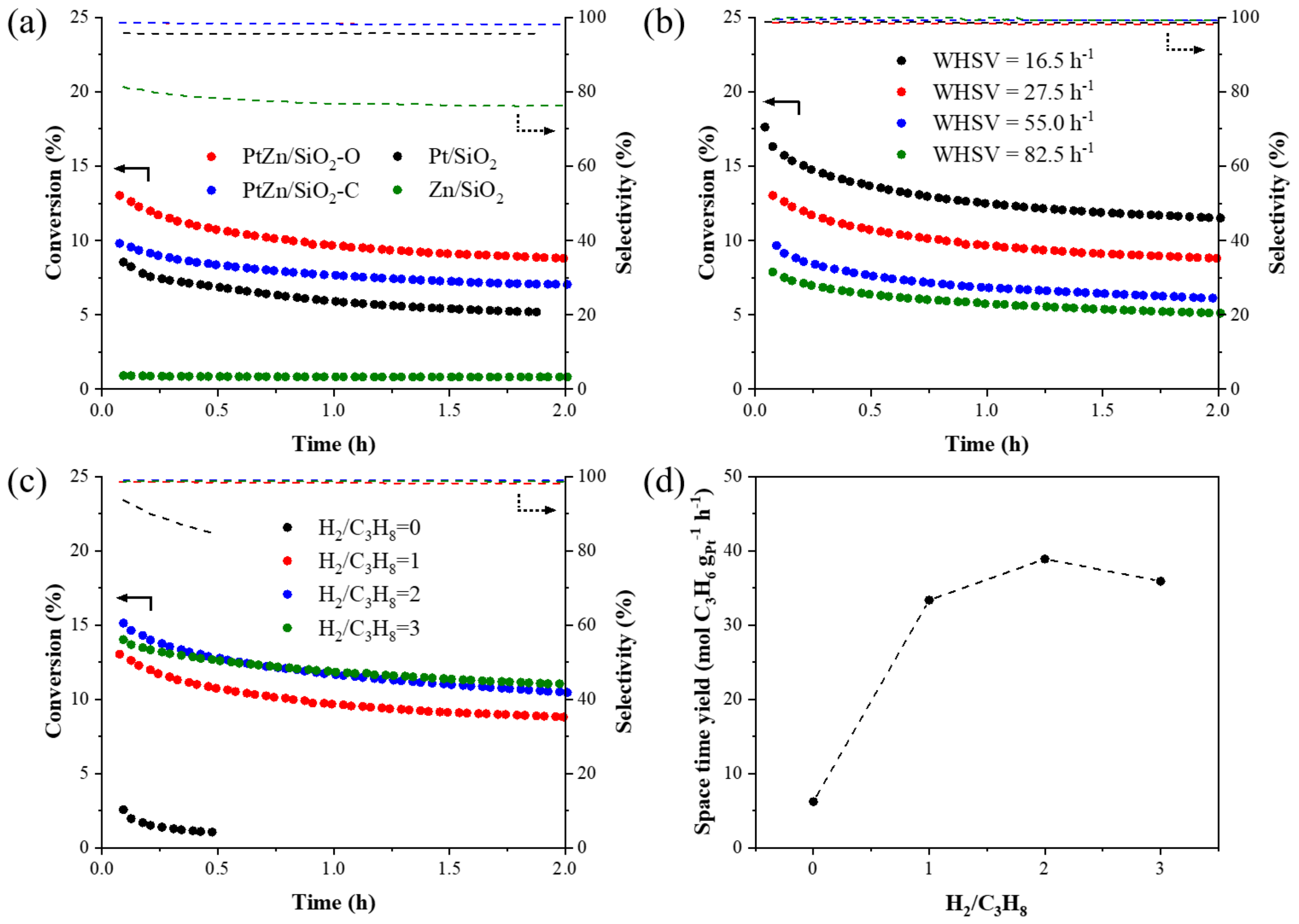

Figure 3. On stream C_3H_8 conversion (solid lines) and C_3H_6 selectivity (dashed lines) as a function of time. (a) Comparison of catalytic performance between PtZn/SiO_2-O, PtZn/SiO_2-C, Pt/SiO_2 and Zn/SiO_2. Reaction conditions: 20 mg catalyst, 20% C_3H_8 + 20% H_2 balanced by Ar, total flow rate 25 mL/min. (b) Influence of weight hourly space velocity (WHSV) on PtZn/SiO_2-O catalytic performance. Reaction conditions: 20 mg catalyst, 20% C_3H_8 + 20% H_2 balanced by Ar, total flow rate 15/25/50/75 mL/min. (c) Influence of H_2/C_3H_8 ratio on PtZn/SiO_2-O catalytic performance. Reaction conditions: 20 mg catalyst, 20% C_3H_8 + 0%/20%/40%/60% H_2 balanced by Ar, total flow rate 25 mL/min. (d) Initial space time yield of C_3H_6 measured with various H_2/C_3H_8 ratios.

Table 1. Initial propane dehydrogenation activity of the catalysts involved in this work. Reaction conditions: 20 mg catalyst, 20% C_3H_8 + 20% H_2 balanced by Ar, total flow rate 25 mL/min

Catalyst	Pt (wt%) *	Zn (wt%) *	C_3H_8 conversion (%)	C_3H_6 selectivity (%)	Space time yield (mol C_3H_6 g_{Pt}^{-1} h^{-1})
PtZn/SiO_2-O	0.24	0.09	13.0	98.6	33.4
PtZn/SiO_2-C	0.26	0.09	9.8	98.6	23.2
Pt/SiO_2	0.26	-	8.5	95.8	19.7
Zn/SiO_2	-	0.12	0.9	81.3	-

*The loadings of Pt and Zn were determined by ICP-OES.

The properties of catalysts reflected in previous characterizations were in alignment with their catalytic performance. Benefiting from the enhanced Pt-Zn interaction, the initial conversion of C_3H_8 over PtZn/SiO_2-O surpassed that over PtZn/SiO_2-C by 30% (Figure 3a and Table 1). The initial space time yield of C_3H_6, normalized by Pt loading, turned out to be similar for PtZn/SiO_2-C and Pt/SiO_2, due to the limited Zn reduction. In contrast, the initial space time yield was increased to 33.4 mol C_3H_6 g_{Pt}^{-1} h^{-1} for PtZn/SiO_2-O, highlighting the distinctive contribution from Zn at the same loading. Subsequently, the most effective catalyst PtZn/SiO_2-O was then tested under various reaction conditions. The first set of tests were to change gas flow rates without modifying the composition (Figure 3b). Despite a gradual decrease in C_3H_8 conversion with increased WHSV, the selectivity to C_3H_6 remained above 98%. In the second set of tests, the amount of co-feeding H_2 was adjusted while maintaining a constant C_3H_8 flow rate. The activity and stability of PtZn/SiO_2-O in these catalytic processes were presented in Figures 3c and 3d. The introduction of H_2 significantly improved C_3H_8 conversion, as product C_3H_6 could be effectively desorbed from the Pt sites, providing space for the next reactant.[24] Furthermore, the undesired coking process was suppressed, lowering the deactivation coefficient from 0.106 h^{-1} for $H_2/C_3H_8=2$ to 0.068 h^{-1} for $H_2/C_3H_8=3$. However, excessive H_2 led to intensive reverse reaction, *i.e.*, C_3H_6 hydrogenation to C_3H_8. Constrained by thermodynamic equilibrium, the C_3H_8 conversion dropped to 14.0% when the H_2/C_3H_8 ratio was set at 3.

Conclusions

In summary, we used an oxalate-bridged Pt-Zn complex to improve the impregnation method, producing size-controlled alloy nanoparticles on SiO_2 support for propane dehydrogenation reaction. During synthesis, the formation of Pt-Zn complex was confirmed by FTIR spectra analysis. Furthermore, TPR and CO-DRIFTS results provided evidence of enhanced alloy formation and charge transfer from Zn to Pt after reduction. HAADF-STEM images showed the prevailing species were amorphous particle around 1 nm, accompanied by some 2-5 nm sized particles. EDS analysis also verified the alloy formation in the nanoparticles formed. Consequently, the complex-derived PtZn/SiO_2 catalyst exhibited a 30% higher conversion of propane and a 40% higher space time yield of propylene compared to the control sample. Co-feeding H_2 was found also important for the reaction. When H_2/C_3H_8 ratio was 2, facilitated propylene desorption led to the highest propane conversion. Further increase in H_2 concentration, however, lowered the thermodynamic equilibrium and finally limited conversion. These findings highlight the important role of metal-metal interactions in the formation of alloy nanoparticles. Using molecular complexes as precursors could thus be a powerful tool in future pursuit of controlled alloy nanoparticle synthesis, of application in catalytic processes such as propane dehydrogenation.

Experimental Section

Catalyst preparation. PtZn/SiO_2-O was synthesized by loading pre-formed oxalate-bridged Pt-Zn complex[16] onto SiO_2 support, followed by *in situ* 20% H_2 reduction at 550℃ for 1 hour before propane dehydrogenation reaction. To prepare the oxalate-bridged Pt-Zn complex, $Zn(NO_3)_2{\cdot}6H_2O$ (Alfa Aesar, 98%), $Pt(NH_3)_4Cl_2{\cdot}xH_2O$ (Sigma Aldrich, 98%) and $(NH_4)_2C_2O_4{\cdot}H_2O$ (Sigma Aldrich, ≥99%) were dissolved in deionized water separately. Then 0.2 mL $Zn(NO_3)_2$ (0.064 M) solution was mixed with $(NH_4)_2C_2O_4$ (0.076 M) solution. If the molar amount of $(NH_4)_2C_2O_4$ equaled that of $Zn(NO_3)_2$, a white precipitate (ZnC_2O_4) would form, which was collected for FTIR analysis. Alternatively, when two more folds of $(NH_4)_2C_2O_4$ was added, the mixture turned out to be clear solution.

Subsequently, 0.2 mL $Pt(NH_3)_4Cl_2$ (0.064 M) was introduced to the mixture, and an oxalate-bridging process immediately took place, leading to precipitation. Finally, 0.02 mL $NH_3{\cdot}H_2O$ solution (Sigma Aldrich, 28-30% NH_3 basis) and 0.4 mL deionized water were used to redissolve the oxalate-bridged Pt-Zn complex, so that it could be loaded onto 0.8 g SiO_2 gel (pore size 60 Å, 70-230 mesh) through impregnation and dried in an oven overnight prior to reduction, reaction and characterizations.

PtZn/SiO_2-C was prepared by a co-impregnation method followed by *in situ* 20% H_2 reduction at 550 ℃ for 1 hour before the propane dehydrogenation reaction. The mixture for impregnation was made up of 0.2 mL $Zn(NO_3)_2$ (0.064 M) solution, 0.2 mL $Pt(NH_3)_4Cl_2$ (0.064 M) solution, 0.92 mL deionized water and 0.8 g SiO_2 gel. Similarly, Pt/SiO_2 and Zn/SiO_2 were obtained by impregnating only the Pt or Zn precursor onto SiO_2 support, with total volume of solution kept constant. The catalysts were dried in an oven overnight prior to reduction, reaction and characterizations.

Catalyst characterization. Fourier-transform infrared (FTIR) spectra of $Pt(NH_3)_4Cl_2$, ZnC_2O_4 and oxalate-bridged Pt-Zn complex were acquired using an Agilent Cary 660 FTIR spectrometer equipped with attenuated total reflectance accessory. The measurement range spanned from 400 to 4000 cm^{-1}.

Elemental composition of catalysts was determined by Perkin Elmer Avio 500 inductively coupled plasma optical emission spectroscopy (ICP-OES). Solid samples were digested with a mixture of HCl, HNO_3 and HF.

Temperature-programmed reduction (TPR) experiments were carried out on a Thermo Scientific TPDRO 1100. The dried catalysts underwent treatment by 5% H_2 from 50 °C to 900 °C with a ramp rate of 10 °C/min.

X-ray diffraction (XRD) patterns of SiO_2 and *ex situ* reduced catalysts were recorded on a Bruker D-8 Advance, with 2θ ranging from 10° to 90°.

CO diffuse reflectance infrared spectra (CO-DRIFTS) were acquired on a Nicolet iS50 FT-IR spectrometer. The catalyst was *ex situ* reduced by 20% H_2 at 550 °C for 1 hour beforehand and *in situ* reduced by pure H_2 at 400 °C for 1 hour to remove the passivation layer. After cooling the sample to 30 °C in H_2 atmosphere, the cell was flushed with Ar to collect the background. Subsequently, 5% CO/He was flowed through the cell until CO adsorption saturation according to the spectra. Finally, the cell was flushed with Ar again to record the signal from residual adsorbed CO.

Images of Pt-based nanoparticles and elemental maps were acquired on a JEOL JEM-ARM200CF aberration-corrected scanning transmission electron microscope (STEM) operating at 200 kV. The size distribution of particles was determined from high-angle annular dark field (HAADF) images.

Backscattered electron images of Pt-based nanoparticles were obtained on a Zeiss Sigma 300 field emission scanning electron microscope (FE-SEM) operating at 10 kV.

Catalytic property measurement. The catalytic performance in propane dehydrogenation reaction was evaluated using a fixed bed downflow reactor built in-house. In a typical experiment, 0.02 g catalyst was mixed with 0.98 g sand (Sigma Aldrich, 50-70 mesh), sandwiched by another two layers of sand, each weighing 0.5 g each. The mixture was supported on quartz wool in a quartz tube with7 mm inner diameter.

Prior to reaction, the catalyst was heated to 550 °C at a 10 °C/min ramp rate and retained for 1 h under 10 mL/min H_2 + 40 mL/min Ar flow. After reduction, the inlet gas was switched to 5 mL/min C_3H_8 + 5 mL/min H_2 + 15 mL/min Ar (WHSV = 27.5 h^{-1}). WHSV (weight hourly space velocity) was defined as the mass flow rate of C_3H_8 divided by the mass of catalyst. The influence of WHSV was studied by varying the total flow rate with the concentration of each gas component kept the same (20% C_3H_8 + 20% H_2 + 60% Ar). The effect of H_2/C_3H_8 ratio was revealed by adjusting the flow rates of H_2 and Ar, while the flow rate of C_3H_8 (5 mL/min) and the total flow rate (25 mL/min) remained constant.

The composition of outlet gas was analyzed by online gas chromatography (Agilent 990 Micro GC) equipped with parallel PoraPLOT Q and MS5A columns and corresponding thermal conductivity detectors, using He and

Ar as carrier gas, respectively. Volumetric fractions of C_3H_8, C_3H_6 and potential by-products, including CH_4, C_2H_6, C_2H_4 and C_2H_2, were determined through external standard calibration. Conversion of C_3H_8 and selectivity to C_3H_6 were calculated by Eqs. 1 and 2, where [Gas] represented the molar flow rate of the gaseous components. Carbon mass balance was defined as the ratio of C atoms in outlet and inlet gas (Eq. 3). Throughout the analysis, carbon mass balance was over 97%. Space time yield of C_3H_6 was defined as the molar flow rate of C_3H_6 in outlet gas divided by the mass of Pt, as shown in Eq. 4. Deactivation of catalysts was characterized according to pseudo first order model (Eq. 5), where X and X_0 represented conversion at time t and the beginning of reaction, respectively. Deactivation coefficient k_d was obtained by liner fitting.

$$\text{Conversion} = \frac{3\times[C_3H_6]_{out} + 2\times[C_2H_6]_{out} + 2\times[C_2H_4]_{out} + 2\times[C_2H_2]_{out} + [CH_4]_{out}}{3\times[C_3H_8]_{out} + 3\times[C_3H_6]_{out} + 2\times[C_2H_6]_{out} + 2\times[C_2H_4]_{out} + 2\times[C_2H_2]_{out} + [CH_4]_{out}} \quad (1)$$

$$\text{Selectivity} = \frac{3\times[C_3H_6]_{out}}{3\times[C_3H_6]_{out} + 2\times[C_2H_6]_{out} + 2\times[C_2H_4]_{out} + 2\times[C_2H_2]_{out} + [CH_4]_{out}} \quad (2)$$

$$\text{Carbon mass balance} = \frac{3\times[C_3H_8]_{out} + 3\times[C_3H_6]_{out} + 2\times[C_2H_6]_{out} + 2\times[C_2H_4]_{out} + 2\times[C_2H_2]_{out} + [CH_4]_{out}}{3\times[C_3H_8]_{in}} \quad (3)$$

$$\text{Space time yield} = \frac{[C_3H_6]_{out}}{m_{Pt}} \quad (4)$$

$$\text{Deactivation model } k_d t = \ln\left(\frac{1-X}{X}\right) - \ln\left(\frac{1-X_0}{X_0}\right) \quad (5)$$

Acknowledgements

Q. He acknowledges the support from National Research Foundation (NRF) Singapore under its NRF Fellowship (NRF-NRFF11-2019-0002), and Singapore Low-Carbon Energy Research Funding Initiative hosted under A*STAR (Proposal ID: LCERFI01-0017; Award No. U2102d2005; Proposal ID: LCERFI01-0033, Award No. U2102d2006).

Supplementary Material

Additional images (HAADF-STEM, SEM-BSD) are given in the supplementary material associated with this manuscript.

References

1. Ye, C.; Peng, M.; Wang, Y.; Zhang, N.; Wang, D.; Jiao, M.; Miller, J. T. *ACS Appl. Mater. Interfaces* **2020,** *12*, 25903-25909.
   https://doi.org/10.1021/acsami.0c05043
2. Wang, Q.; Tichit, D.; Meunier, F.; Guesmi, H. *J. Phys. Chem. C* **2020,** *124*, 9979-9989.
   https://doi.org/10.1021/acs.jpcc.0c01296

3. Zhang, J.; Deng, Y.; Cai, X.; Chen, Y.; Peng, M.; Jia, Z.; Jiang, Z.; Ren, P.; Yao, S.; Xie, J. *ACS Catal.* **2019,** *9,* 5998-6005.
   https://doi.org/10.1021/acscatal.9b00601
4. Chen, S.; Zhao, Z.-J.; Mu, R.; Chang, X.; Luo, J.; Purdy, S. C.; Kropf, A. J.; Sun, G.; Pei, C.; Miller, J. T. *Chem* **2021,** *7*, 387-405.
   https://doi.org/10.1016/j.chempr.2020.10.008
5. Motagamwala, A. H.; Almallahi, R.; Wortman, J.; Igenegbai, V. O.; Linic, S. *Science* **2021,** *373*, 217-222.
   https://doi.org/10.1126/science.abg7894
6. Zhang, X.; He, N.; Liu, C.; Guo, H. *Catal. Lett.* **2019,** *149*, 974-984.
   https://doi.org/10.1007/s10562-019-02671-4
7. Chen, S.; Chang, X.; Sun, G.; Zhang, T.; Xu, Y.; Wang, Y.; Pei, C.; Gong, J. *Chem. Soc.Rev.* **2021,** *50*, 3315-3354.
   https://doi.org/10.1039/D0CS00814A
8. Yang, M.-L.; Zhu, Y.-A.; Zhou, X.-G.; Sui, Z.-J.; Chen, D. *ACS Catal.* **2012,** *2*, 1247-1258.
   https://doi.org/10.1021/cs300031d
9. Filez, M.; Redekop, E. A.; Galvita, V. V.; Poelman, H.; Meledina, M.; Turner, S.; Van Tendeloo, G.; Bell, A. T.; Marin, G. B. *Phys. Chem. Chem. Phys.* **2016,** *18*, 3234-3243.
   https://doi.org/10.1039/C5CP07344H
10. Qi, L.; Babucci, M.; Zhang, Y.; Lund, A.; Liu, L.; Li, J.; Chen, Y.; Hoffman, A. S.; Bare, S. R.; Han, Y.; Gates, B. C.; Bell, A. T. *J. Am. Chem. Soc.* **2021,** *143*, 21364-21378.
    https://doi.org/10.1021/jacs.1c10261
11. Qi, L.; Zhang, Y.; Babucci, M.; Chen, C.; Lu, P.; Li, J.; Dun, C.; Hoffman, A. S.; Urban, J. J.; Tsapatsis, M.; Gates, B. C.; Bell, A. T. *ACS Catal.* **2022,** *12*, 11177-11189.
    https://doi.org/10.1021/acscatal.2c01631
12. Searles, K.; Chan, K. W.; Mendes Burak, J. A.; Zemlyanov, D.; Safonova, O.; Copéret, C. *J. Am. Chem. Soc.* **2018,** *140*, 11674-11679.
    https://doi.org/10.1021/jacs.8b05378
13. Ryoo, R.; Kim, J.; Jo, C.; Han, S. W.; Kim, J.-C.; Park, H.; Han, J.; Shin, H. S.; Shin, J. W. *Nature* **2020,** *585*, 221-224.
    https://doi.org/10.1038/s41586-020-2671-4
14. Chang, X.; Zhao, Z.-J.; Lu, Z.; Chen, S.; Luo, R.; Zha, S.; Li, L.; Sun, G.; Pei, C.; Gong, J. *Nature Nanotechnology* **2023**, 1-6.
    https://doi.org/10.1038/s41565-023-01344-z
15. Xu, C.; Tan, S.; Tang, Y.; Xi, S.; Yao, B.; Wade, A.; Zhao, B.; Lu, S.; Du, Y.; Tian, M. *Appl. Catal. B: Environmental* **2024,** *341*, 123285.
    https://doi.org/10.1016/j.apcatb.2023.123285
16. Zadesenets, A.; Filatov, E. Y.; Yusenko, K.; Shubin, Y. V.; Korenev, S.; Baidina, I. *Inorg. Chim. Acta* **2008,** *361*, 199-207.
    https://doi.org/10.1016/j.ica.2007.07.006
17. Salado-Leza, D.; Porcel, E.; Yang, X.; Štefančíková, L.; Bolsa-Ferruz, M.; Savina, F.; Dragoe, D.; Guerquin-Kern, J.-L.; Wu, T.-D.; Hirayama, R. *Nanotechnol. Sci. Appl.* **2020**, 61-76.
    https://doi.org/10.2147/NSA.S257392
18. Yang, X.; Salado-Leza, D.; Porcel, E.; González-Vargas, C. R.; Savina, F.; Dragoe, D.; Remita, H.; Lacombe, S. *Int. J. Mol. Sci.* **2020,** *21*, 1619.

https://doi.org/10.3390/ijms21051619

19. Sood, S.; Kumar, A.; Sharma, N. *ChemistrySelect* **2016,** *1*, 6925-6932.
https://doi.org/10.1002/slct.201601435
20. Garidzirai, R.; Modisha, P.; Shuro, I.; Visagie, J.; van Helden, P.; Bessarabov, D. *Catalysts* **2021,** *11*, 490.
https://doi.org/10.3390/catal11040490
21. Pourzolfaghar, H.; Abnisa, F.; Wan Daud, W. M. A.; Aroua, M. K.; Mahlia, T. M. I. *Energies* **2020,** *13*, 2802.
https://doi.org/10.3390/en13112802
22. Murata, K.; Kurimoto, N.; Yamamoto, Y.; Oda, A.; Ohyama, J.; Satsuma, A. *ACS Appl. Nano Mater.* **2021,** *4*, 4532-4541.
https://doi.org/10.1021/acsanm.1c00128
23. Wan, H.; Qian, L.; Gong, N.; Hou, H.; Dou, X.; Zheng, L.; Zhang, L.; Liu, L. *ACS Catal.* **2023,** *13*, 7383-7394.
https://doi.org/10.1021/acscatal.3c00548
24. Saerens, S.; Sabbe, M. K.; Galvita, V. V.; Redekop, E. A.; Reyniers, M.-F.; Marin, G. B. *ACS Catal.* **2017,** *7*, 7495-7508.
https://doi.org/10.1021/acscatal.7b01584